Coherent Electron Transfer at the Ag/Graphite Heterojunction Interface

Shijing Tan,[1,2] Yanan Dai,[1] Shengmin Zhang,[1] Liming Liu,[3] Jin Zhao,[1,3,4,*] and Hrvoje Petek[1,†]

[1]*Department of Physics and Astronomy and Pittsburgh Quantum Institute, University of Pittsburgh, Pittsburgh, Pennsylvania 15260, USA*
[2]*Hefei National Laboratory for Physical Sciences at the Microscale, and Department of Chemical Physics, University of Science and Technology of China, Hefei, Anhui 230026, China*
[3]*ICQD/Hefei National Laboratory for Physical Sciences at the Microscale, and Key Laboratory of Strongly-Coupled Quantum Matter Physics, Chinese Academy of Sciences, and Department of Physics, University of Science and Technology of China, Hefei, Anhui 230026, China*
[4]*Synergetic Innovation Center of Quantum Information & Quantum Physics, University of Science and Technology of China, Hefei, Anhui 230026, China*

Charge transfer in transduction of light to electrical or chemical energy at heterojunctions of metals with semiconductors or semimetals is believed to occur by photogenerated hot electrons in metal undergoing incoherent internal photoemission through the heterojunction interface. Charge transfer, however, can also occur coherently by dipole coupling of electronic bands at the heterojunction interface. Microscopic physical insights into how transfer occurs can be elucidated by following the coherent polarization of the donor and acceptor states on the time scale of electronic dephasing. By time-resolved multiphoton photoemission spectroscopy (MPP), we investigate the coherent electron transfer from an interface state that forms upon chemisorption of Ag nanoclusters onto graphite to a σ symmetry interlayer band of graphite. Multidimensional MPP spectroscopy reveals a resonant two-photon transition, which dephases within 10 fs completing the coherent transfer.

Photoinduced charge transfer is a fundamental process in transduction of light to chemical and electrical energy in natural and artificial light harvesting [1–5], which has been studied in the context of surface photochemistry, plasmonically enhanced photocatalysis, molecule sensitized solar energy conversion, etc. [1,2,6–27]. In the prevailing scheme for interfacial charge transfer [Fig. 1(a)], photon absorption excites hot electrons in a metal by a direct or plasmon enhanced absorption, which thereafter transfer over a Schottky barrier to the semiconductor by incoherent transport or under influence of an applied potential [1,4,15,22,28]. In this internal photoemission scenario, the efficiency of energy harvesting is low because only a fraction of hot electrons acquires the necessary energy and momentum to overcome the interfacial potential and populate the semiconductor, while competing electron-electron (e-e) and electron-phonon (e-p) scattering processes remove energy from hot electrons [2,11,14,17,18,29]. Alternatively, interfacial charge transfer can also occur by coherent coupling of the donor and acceptor states [5,9,18–23,30]. The electric dipole interaction is instantaneous [31], so the electric charge can redistribute across an interface on the time scale of dephasing of the optically excited coherence [5,6,9,18–22,30]. Therefore, the dipole coupling enables coherent electron transfer across an interface with minimal loss of energy or population [Fig. 1(b)].

Ultrafast charge transfer can be studied by ultrafast optical techniques such as transient absorption [8,16,20,22], second harmonic generation (SHG) [13,17], photoelectron spectroscopy, and microscopy [6,9,11,17,24,26], etc., or by evaluating linewidths in the electronic spectroscopy [32,33]. Few methods, however, can directly probe the quantum superposition states that are involved in the coherent charge transfer [3,5,6,31]. Although, several experiments and theory have claimed direct photoinduced electron transfer at complex interfaces [20–23], detecting the coherent polarization of the donor and acceptor states in the act of transfer at chemical and solid-state heterojunctions requires direct methods such as coherent multidimensional electronic spectroscopy [3,5,31].

In this Letter, we deploy the coherent interferometric time-resolved MPP (M refers to the multiphotonic order) spectroscopy and density functional theory to study the photoinduced electron dynamics within Ag nanocluster-decorated graphite (Gr) heterojunctions [31,34–36]. A resonant two-photon transition is found for photon energy of $\hbar\omega =$ ~ 2.09 eV, which excites electrons from an occupied Ag chemisorption-induced interface state (IFS) to the unoccupied σ-symmetry interlayer band (ILB) of Gr [Figs. 1(c) and 1(d)] [35,37,38]. The electronic transition drives the coherent electron transfer, which occurs within ~ 10 fs by electronic dephasing of the coupled bands.
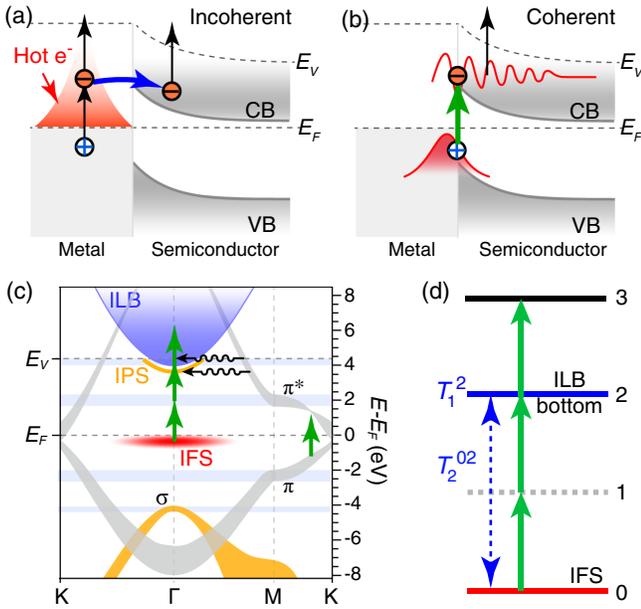
FIG. 1.   The incoherent internal photoemission (a) and coherent (b) photoinduced charge transfer schemes at the metal-semiconductor interface and their detection by 2PP spectroscopy. (c) The $k_\parallel$ band structure of Gr, with the Ag chemisorption induced occupied IFS. The green arrows indicate the MPP excitation involving the resonant two-photon transition from IFS to ILB. The wavy arrows indicate the phonon assisted electron scattering from the π^* band of Gr. The widths of the bands convey their perpendicular dispersions. (d) The four-level excitation scheme in 3PP process including the initial state "0" (IFS), the virtual intermediate state "1", the penultimate state "2" (ILB), and the final photoemission continuum "3". The T_1^2 represent the effective hot electron lifetime and T_2^{02} the polarization dephasing time between the IFS and ILB.

The ILB is uniquely a 3D nearly free-electron band of quasi-2D van der Waals crystals like Gr; it has characteristic nonnuclear density maxima between the basal planes, which reflect its origin in hybridization of the image potential states (IPSs) of the component sheets [39,40]. In addition to the in-plane IPS-like dispersion, the strong interplane interactions cause the ILB to disperse perpendicular to the basal planes between the Γ and A points from ~4.0 to 7.0 eV [Fig. 1(c)] [38]; its existence has been established by the inverse photoemission and x-ray absorption spectroscopy [37,38], but a band gap of ~8 eV at the Γ point puts it out of reach of optical spectroscopy with VIS-near-UV light. In a recent study we reported on the multiphoton thermionic emission upon the π-π^* excitation of Gr with IR-VIS light [35]. The optical excitation of hot electrons, causes e-e scattering among them through the weakly screened Coulomb interaction; this generates a hot thermal electron distribution (up to 5500 K) within <25 fs, which is sufficiently hot to populate the ILB to above the vacuum level E_V, where some electrons undergo thermionic emission.

We also performed a 2PP study of the plasmonically enhanced photodynamics of Ag nanocluster decorated Gr with UV excitation [36]. A significant contribution to 2PP spectra was found from the chemisorption-induced IFS with a maximum at ~0.2 eV below the Fermi level, E_F, which forms upon chemisorption when Ag 5s orbitals donate electrons to π orbitals of Gr [27]. We report that in Ag/Gr coherent charge transfer occurs from the IFS to the ILB by two-photon absorption of visible light.

The Ag nanocluster decorated Gr sample was formed and characterized by the same methods as in our recent studies [27,36]. MPP spectra are excited with a tunable 520–700 nm ($\hbar\omega = 2.38$-1.77 eV) light pulses from a noncollinear parametric amplifier, which is pumped by a Yb-doped fiber laser (Clark-MXR Impulse), to produce <20 fs excitation pulses at a 1 MHz repetition rate. A hemispherical electron analyzer records 2D spectra of photoelectron counts vs the final state energy, E_{final} (relative to the E_F) and parallel momentum $k_\parallel$ [31,41]. A Mach-Zehnder interferometer generates identical pump-probe pulses for measurement of photoemission interferograms, where the photoelectron counts vs E_{final} and $k_\parallel$ are recorded while the pump-probe delay τ is scanned in <0.1 fs steps [27,31] (see the Supplemental Material for more details [42]).

Figures 2(a) and 2(b) show the changes in MPP spectra when excited with p- and s-polarized $\hbar\omega = 2.0$ eV light at $k_\parallel = 0$ Å^{-1} as Ag atoms are deposited to form Ag nanoclusters [oblate with an average diameter and height of 5.3 ± 1.1 and 1.2 ± 0.4 nm; density in the range of 0.3-1.8($\times 10^{12}$) cm^{-2}] on the Gr surface [36]. The MPP spectra of the clean Gr (red lines) for both p- and s-polarized excitation are dominated by the thermionic emission with an exponentially decreasing intensity above E_V. With p polarization there is an additional peak for the $n = 1$ IPS at 3.6 eV above the E_F [35].

As displayed in Figs. 2(a) and 2(b), forming the Ag nanoclusters significantly *reduces* the MPP yields relative to the clean Gr surface, with only minor changes in the spectral profiles. The MPP signal decrease indicates that, contrary to the UV excitation [36], with the visible excitation there is no plasmonic enhancement of absorption and the dominant thermionic emission of Gr is suppressed (Supplemental Material [42]). This is because Ag chemisorption increases the density of states (DOS) near E_F, thereby enhancing screening of the Coulomb interaction, and consequently suppressing the e-e scattering among hot electrons [35].

A new result of Ag deposition is a peak that appears only with the p-polarized visible excitation at $E_{\mathrm{final}} \sim 0.4$ eV above the IPS [the blue arrow in Fig. 2(a) and Supplemental Material [42]]. This peak is the primary focus of our study, and will be assigned to the ILB.

Because for the bare Gr, we found an unconventional power-law dependence of MPP spectra on the laser fluence, I^M, where M increases from 3 to 8 as $\hbar\omega$ decreases from
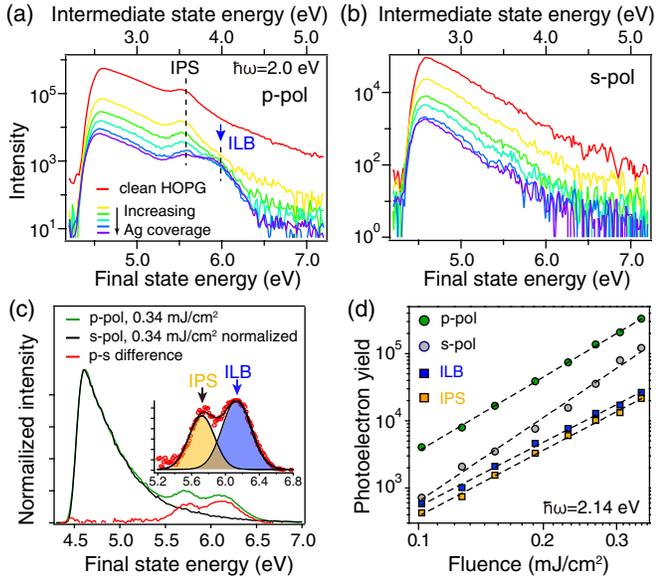
FIG. 2. MPP spectra with *p*- (a) and *s*-polarized (b) $\hbar\omega = 2.0$ eV excitation obtained at the Gr surface for sequential Ag deposition. The blue arrow marks the new state, i.e., the ILB. (c) The normalized *s*- and *p*-polarized spectra at Ag/Gr with $\hbar\omega = 2.14$ eV and $I = 0.34$ mJ/cm² excitation, and their difference spectrum (red); the inset shows the Gaussian fitting of the IPS and ILB components of the difference spectrum. (d) The log-log plots of photoelectron yields for the *p*- and *s*-polarized spectra, the IPS, and ILB components vs *I* for $\hbar\omega = 2.14$ eV. The dashed lines indicate slopes of 3.7 ± 0.1 and 4.2 ± 0.2 for the *p*- and *s*-polarized spectra, and 3.3 ± 0.1 and 3.1 ± 0.1 for the IPS and ILB.

FIG. 3. (a) A series of normalized 3PP spectra at Ag/Gr surface excited with *p*-polarized $\hbar\omega = 1.79$-2.24 eV (693–553 nm) light. The inset shows details of the IPS and ILB peaks near the IFS-ILB resonance. The blue dashed line traces the resonance behavior of the ILB. (b) The plots of the E_{final} of IPS and ILB vs $\hbar\omega$; the slopes of ~1 and intercepts confirm them to be penultimate states in 3PP with energies of 3.60 and 4.0 eV, respectively. (c) The plot of intensity ratio between ILB and secondary electron yield vs $\hbar\omega$.

2.4 to 1.4 eV [35], to determine the excitation mechanism we first examine the power law dependence of MPP spectra of the Ag/Gr surface. By varying *I* to measure the MPP spectra with *p*- and *s*-polarized $\hbar\omega = 2.14$ eV excitation, the IPS and ILB component strengths are established by fitting the *p*-*s* difference spectra with Gaussian profiles (Fig. 2(c) and Supplemental Material [42]). The total yields of the *p*- and *s*-excited spectra as well as the area under the fit of the IPS and ILB components are plotted vs *I* in Fig. 2(d). The slopes of the log-log plots of the total yields gives $M = \sim 3.7$ and ~ 4.2 for the *p* and *s* excitation, which is consistent with $M = \sim 4.1$ for the thermionic emission from the bare Gr [35]. For the IPS and ILB components, however, we obtain $M = \sim 3.3$ and ~ 3.1, respectively, as expected for a conventional, ladder climbing three-photon MPP process. Measurements for other $\hbar\omega$ confirm this trend (Supplemental Material [42]).

To scrutinize how the ILB is excited, in Fig. 3(a) we report the photon energy dependent 3PP spectra in the range of $\hbar\omega = 1.79$-2.24 eV. The final state energies of ILB and IPS are plotted vs $\hbar\omega$ in Fig. 3(b); their slopes of ~1 and intercepts of 3.60 and 4.0 eV above E_F show that they are penultimate states detected by absorbing one more photon after their occupation by two-photon absorption. 4.0 eV agrees with the previous reports of the ILB band

minimum at the Γ point [37,38], as shown in Fig. 1(c). This extra peak cannot be assigned to the $n = 2$ IPS, which is known to be 0.75 eV above the $n = 1$ IPS and have much lower intensity [54]. In MPP spectra of the clean Gr, the Γ point of ILB does not appear because there is no initial state from where it can be excited [35]. Ag nanocluster chemisorption introduces the initial state IFS DOS just below E_F at the Γ point that enables the bottom of ILB to be excited via the two-photon near-resonant excitation.

To confirm that there is a resonant IFS-ILB two-photon transition, we plot 3PP spectra normalized to the secondary electron yield vs $\hbar\omega$ in Fig. 3(c). The two-photon resonance maximizes the ILB intensity at $\hbar\omega = 2.09$ eV, locating the initial state at ~0.18 eV below E_F, precisely the energy of IFS with UV excitation [36]; this establishes the two-photon resonance enhancement of the IFS-ILB excitation. By contrast, the IPS is not enhanced [Fig. 3(a)], because it is populated thermionically.

Next, we calculate the transition matrix element $T^{i}_{n'n}(k) = \langle \Psi_{n'k} | \vec{r}_i \cdot \vec{E} | \Psi_{nk} \rangle$ for the IFS–ILB transition by density functional theory (Supplemental Material [42]). We obtain the wave functions for the coupled bands in Figs. 4(a)–4(d), from the electronic structure of an array of Ag trimers on a 10-layer-thick Gr [36]. The calculations predict three transitions within the range of our measurements [Fig. 4(e)]. At the Γ point we find two transitions from IFS at 3.30 and 3.65 eV above E_F to states with characteristic spatial
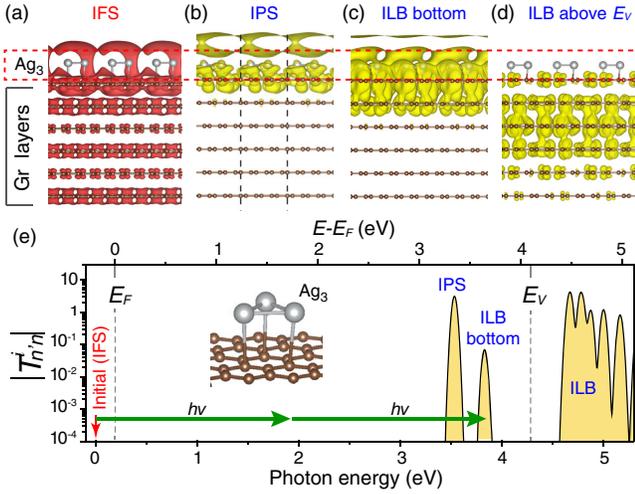
FIG. 4. (a)–(d) The spatial distributions (side view) of the bands involved in the optical transitions. (e) The calculated transition dipole moment amplitudes, $|T^i_{n'n}|$ (broadened with Gaussian functions) from the initial IFS to unoccupied states at the Γ point for an Ag$_3$ array on a ten-layer-thick Gr stack, as shown in the inset. The bottom axis represents the total photon energy and the upper axis the energy of coupled states relative to E_F.

distributions of IPS and ILB, as shown in Figs. 4(b) and 4(c). If evaluated relative to E_F, the calculated energies are 0.35 eV below the observed ones, because the final state energies are defined with respect to E_V, and the calculated work function $\Phi = E_V - E_F = 4.05$ eV is 0.35 eV below experiment, probably because the small Ag$_3$ clusters have relatively large charge transfer to Gr. Imposing periodic boundary conditions on Gr slab causes the ILB to break up into quantum well states (Supplemental Material [42]). The additional transition moments above 4.45 eV [Fig. 4(e)] involve such quantum well states, which do not exist in the bulk experimental sample, so they are not observed.

Although our calculated transition moments are for the linear excitation, we note that they make the dominant contributions to the second-order transition moments for a two-photon IFS-ILB excitation. The calculation with Ag$_3$ clusters also predicts a large transition moment for the IFS-IPS excitation, which is not observed. For larger clusters, as used in the experiment, however, there is little spatial overlap between the IFS at the Ag/Gr interface, and the IPS, which is confined to the bare Gr surface.

The most direct method, however, to confirm the coherent resonant IFS-ILB transition is to record coherences in photoemission interferograms [31,41], such as in Fig. 5(a) for $k_\parallel = 0$ Å^{-1}, which is taken with $\hbar\omega = 2.05$ eV. We find that interference fringes for the IFS-ILB resonance ($E_{\text{final}} \sim 6.1$ eV) tilt and curve as τ increases from 0 fs [expanded data in Fig. 5(a)]. Tilting of fringes implies that the signal at a particular E_{final} correlates with the spectral distribution of the induced coherences in the sample [31].

For a more direct signature of coherence in the 3PP process, we Fourier transform (FT) the interferogram
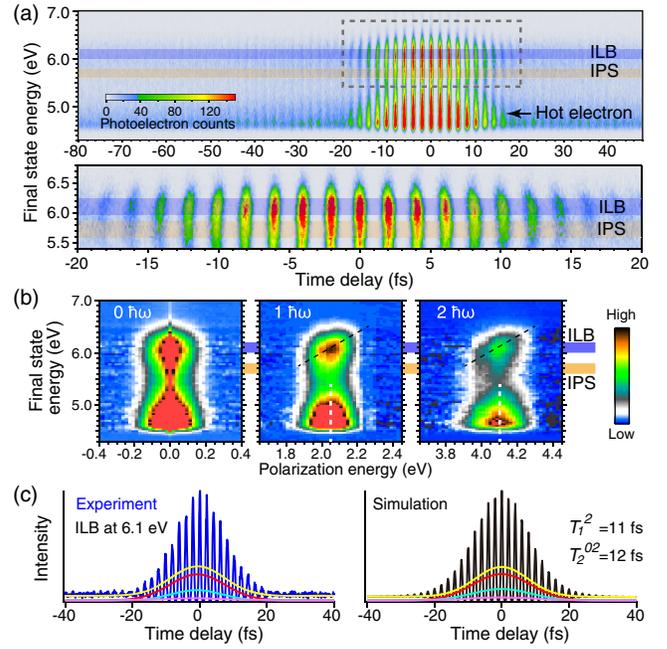
FIG. 5. (a) Interferogram of the photoelectron counts vs the E_{final} and pump-probe time delay τ measured with p-polarized $\hbar\omega = 2.05$ eV light for Ag/Gr at $k_\parallel = 0$ Å^{-1}. The data in the dashed rectangle are enlarged in the lower panel. (b) 2D photoelectron spectra obtained by Fourier transforming the interferogram in (a). The vertical dashed lines indicate the photon energies, and the black dashed lines indicate the slope of 2. (c) Left panel: experimental I2PC trace obtained at the cross section in (a) at 6.1 eV. Right panel: simulated I2PC trace with the four-level OBE approach [Fig. 1(d)]. The I2PCs are decomposed into phase average (yellow), the envelopes of the 1ω (red), 2ω (cyan), and 3ω (pink) oscillatory components, which are used to fit the polarization and population decay parameters [41].

[Fig. 5(a)] with respect to time to generate a spectrum of E_{final} (ordinate) vs the polarization energy (abscissa) [31,41]. The FT has components at dc ($0\hbar\omega$), and first ($1\hbar\omega$) and second ($2\hbar\omega$) harmonics of the driving field, as shown in Fig. 5(b) ($3\hbar\omega$ is too weak to analyze). The $0\hbar\omega$ component has contributions from the incoherent hot electron population dynamics, whereas the $1\hbar\omega$ and $2\hbar\omega$ components characterize the linear and second-order nonlinear coherences. The FTs for the ILB at $1\hbar\omega$ and $2\hbar\omega$ are tilted, as expected from tilting of the fringes; the slope of ~ 2 for the ILB [the black dashed line in Fig. 5(b)] is consistent with a coherent two-photon absorption [31].

Finally, we determine the dephasing rate of the coherent polarization in the IFS-ILB excitation. From the horizontal cross section at $E_{\text{final}} = 6.1$ eV (IFS-ILB transition) through Fig. 5(a), we obtain an interferometric two pulse correlation (I2PC) trace in Fig. 5(c). The I2PC is modeled with an optical Bloch equation (OBE) approach [41,55,56] for a four-level scheme in Fig. 1(d). The simulation gives a population lifetime of $T_1^2 = 11$ fs and dephasing time of $T_2^{02} = 12$ fs for the IFS-ILB coherence. These values are

comparable to the 13 fs duration of the excitation pulse (Supplemental Material [42]), but because the OBE is a crude model for a bulk sample, we estimate of ± 5 fs, based on model dependent variations. Nevertheless, the OBE simulation supports that the coherent electron transfer at Ag/Gr interface is completed within ~ 10 fs. The dephasing time probably also has contributions from the inhomogeneous broadening of both the IFS and ILB, particularly because the ILB is dispersive so, although the DOS at the Γ point is the largest, the optical transition may couple to states with other perpendicular momenta. The value of $T_1^2 = 11$ fs is less significant, because the incoherent signal at $E_{\text{final}} = 6.1$ eV includes the thermionic component, so the signal may probe hot electrons at other energies.

In conclusion, we have used multidimensional coherent photoemission spectroscopy to characterize the ILB of graphite and its excitation by two-photon resonant photo-induced charge transfer from the Ag chemisorption-induced IFS. Our detection and assignment of ILB at 4.0 eV above E_F may explain some features of ultrafast spectroscopy of graphite that have been attributed to renormalization of the π-π^* band gap at high excitation densities [57]. The coherent charge transfer, which is completed by dephasing on ~ 10 fs time scale, is expected to be faster and more efficient than incoherent processes because it precedes electron energy relaxation. By contrast, charge transfer by internal photoemission from the photo-excited hot electron distribution occurs in competition with energy relaxation, and processes that generally belong to the Marcus theory can only be described when a local equilibrium exists [58]. For example, for Au particles, PbSe nanocrystals, and activated TiO_2 surfaces hot electron injection has been reported on <10 fs to hundreds of picoseconds time scales [8,13,16,27,33,59,60], with the fastest processes most likely being coherent. Our study also highlights the ability of the interferometric MPP spectroscopy to characterize ultrafast electronic coherences in solid state materials, and their interfaces, and also provides deep insights into the electron phase and energy dynamics in model metal-semimetal heterojunctions [27].

The authors declare no competing financial interests.

*Corresponding author.
 zhaojin@ustc.edu.cn
†Corresponding author.
 petek@pitt.edu

[1] X.-Y. Zhu, Annu. Rev. Phys. Chem. 53, 221 (2002).
[2] X.-Y. Zhu, J. Phys. Chem. B 108, 8778 (2004).
[3] G. D. Scholes, G. R. Fleming, A. Olaya-Castro, and R. van Grondelle, Nat. Chem. 3, 763 (2011).
[4] A. A. Bakulin, A. Rao, V. G. Pavelyev, P. H. M. van Loosdrecht, M. S. Pshenichnikov, D. Niedzialek, J. Cornil, D. Beljonne, and R. H. Friend, Science 335, 1340 (2012).
[5] G. D. Scholes et al., Nature (London) 543, 647 (2017).
[6] S. Ogawa, H. Nagano, and H. Petek, Phys. Rev. Lett. 82, 1931 (1999).
[7] H. Petek, M. J. Weida, H. Nagano, and S. Ogawa, Science 288, 1402 (2000).
[8] R. Huber, J.-E. Moser, M. Grätzel, and J. Wachtveitl, J. Phys. Chem. B 106, 6494 (2002).
[9] K. Onda, B. Li, J. Zhao, K. D. Jordan, J. Yang, and H. Petek, Science 308, 1154 (2005).
[10] J. T. Yates, Jr. and H. Petek, Chem. Rev. 106, 4113 (2006).
[11] J. Stähler, U. Bovensiepen, M. Meyer, and M. Wolf, Chem. Soc. Rev. 37, 2180 (2008).
[12] H. Petek and J. Zhao, Chem. Rev. 110, 7082 (2010).
[13] W. A. Tisdale, K. J. Williams, B. A. Timp, D. J. Norris, E. S. Aydil, and X.-Y. Zhu, Science 328, 1543 (2010).
[14] S. Linic, P. Christopher, and D. B. Ingram, Nat. Mater. 10, 911 (2011).
[15] M. Galperin and A. Nitzan, Phys. Chem. Chem. Phys. 14, 9421 (2012).
[16] L. Du, A. Furube, K. Hara, R. Katoh, and M. Tachiya, J. Photochem. Photobiol. C 15, 21 (2013).
[17] A. E. Jailaubekov et al., Nat. Mater. 12, 66 (2013).
[18] K. O. Aruda, M. Tagliazucchi, C. M. Sweeney, D. C. Hannah, and E. A. Weiss, Phys. Chem. Chem. Phys. 15, 7441 (2013).
[19] R. Long and O. V. Prezhdo, J. Am. Chem. Soc. 136, 4343 (2014).
[20] S. M. Falke et al., Science 344, 1001 (2014).
[21] M. J. Kale, T. Avanesian, H. Xin, J. Yan, and P. Christopher, Nano Lett. 14, 5405 (2014).
[22] K. Wu, J. Chen, J. R. McBride, and T. Lian, Science 349, 632 (2015).
[23] C. Boerigter, R. Campana, M. Morabito, and S. Linic, Nat. Commun. 7, 10545 (2016).
[24] M. K. L. Man et al., Nat. Nanotechnol. 12, 36 (2017).
[25] H. Petek, Nat. Nanotechnol. 12, 3 (2017).
[26] A. Föhlisch et al., Surf. Sci. 606, 881 (2012).
[27] S. Tan, A. Argondizzo, J. Ren, L. Liu, J. Zhao, and H. Petek, Nat. Photonics 11, 806 (2017).
[28] X. Y. Zhu, Surf. Sci. Rep. 56, 1 (2004).
[29] H. Petek, J. Chem. Phys. 137, 091704 (2012).
[30] A. J. Fleisher, P. J. Morgan, and D. W. Pratt, J. Chem. Phys. 131, 211101 (2009).
[31] X. Cui, C. Wang, A. Argondizzo, S. Garrett-Roe, B. Gumhalter, and H. Petek, Nat. Phys. 10, 505 (2014).
[32] L. Bartels, G. Meyer, K. H. Rieder, D. Velic, E. Knoesel, A. Hotzel, M. Wolf, and G. Ertl, Phys. Rev. Lett. 80, 2004 (1998).
[33] J. Schnadt et al., Nature (London) 418, 620 (2002).

[34] H. Petek and S. Ogawa, Prog. Surf. Sci. **56,** 239 (1997).

[35] S. Tan, A. Argondizzo, C. Wang, X. Cui, and H. Petek, Phys. Rev. X **7,** 011004 (2017).

[36] S. Tan, L. Liu, Y. Dai, J. Ren, J. Zhao, and H. Petek, J. Am. Chem. Soc. **139,** 6160 (2017).

[37] T. Fauster, F. J. Himpsel, J. E. Fischer, and E. W. Plummer, Phys. Rev. Lett. **51,** 430 (1983).

[38] D. A. Fischer, R. M. Wentzcovitch, R. G. Carr, A. Continenza, and A. J. Freeman, Phys. Rev. B **44,** 1427 (1991).

[39] V. M. Silkin, J. Zhao, F. Guinea, E. V. Chulkov, P. M. Echenique, and H. Petek, Phys. Rev. B **80,** 121408 (2009).

[40] M. Feng, J. Zhao, T. Huang, X.-Y. Zhu, and H. Petek, Acc. Chem. Res. **44,** 360 (2011).

[41] S. Zhang, C. Wang, X. Cui, Y. Wang, A. Argondizzo, J. Zhao, and H. Petek, Phys. Rev. B **93,** 045401 (2016).

[42] See the Supplemental Material at http://link.aps.org/supplemental/10.1103/PhysRevLett.120.126801 for additional experimental and computational details, which includes Refs. [43–53].

[43] M. Posternak, A. Baldereschi, A. J. Freeman, E. Wimmer, and M. Weinert, Phys. Rev. Lett. **50,** 761 (1983).

[44] K. Takahashi, M. Imamura, I. Yamamoto, J. Azuma, and M. Kamada, Phys. Rev. B **89,** 155303 (2014).

[45] W. Chen, D. Qi, X. Gao, and A. T. S. Wee, Prog. Surf. Sci. **84,** 279 (2009).

[46] G. Kresse and J. Furthmüller, Phys. Rev. B **54,** 11169 (1996).

[47] G. Kresse and J. Hafner, Phys. Rev. B **48,** 13115 (1993).

[48] J. P. Perdew, M. Ernzerhof, and K. Burke, J. Chem. Phys. **105,** 9982 (1996).

[49] J. P. Perdew, K. Burke, and M. Ernzerhof, Phys. Rev. Lett. **77,** 3865 (1996).

[50] P. E. Blöchl, Phys. Rev. B **50,** 17953 (1994).

[51] G. Kresse and D. Joubert, Phys. Rev. B **59,** 1758 (1999).

[52] J. Harl, L. Schimka, and G. Kresse, Phys. Rev. B **81,** 115126 (2010).

[53] V. Popescu and A. Zunger, Phys. Rev. B **85,** 085201 (2012).

[54] R. Yamamoto, T. Yamada, M. Taguchi, K. Miyakubo, H. S. Kato, and T. Munakata, Phys. Chem. Chem. Phys. **14,** 9601 (2012).

[55] M. J. Weida, S. Ogawa, H. Nagano, and H. Petek, J. Opt. Soc. Am. B **17,** 1443 (2000).

[56] W. Nessler, S. Ogawa, H. Nagano, H. Petek, J. Shimoyama, Y. Nakayama, and K. Kishio, Phys. Rev. Lett. **81,** 4480 (1998).

[57] S. Pagliara, G. Galimberti, S. Mor, M. Montagnese, G. Ferrini, M. S. Grandi, P. Galinetto, and F. Parmigiani, J. Am. Chem. Soc. **133,** 6318 (2011).

[58] J. Stähler, C. Gahl, and M. Wolf, Acc. Chem. Res. **45,** 131 (2012).

[59] O. V. Prezhdo, W. R. Duncan, and V. V. Prezhdo, Prog. Surf. Sci. **84,** 30 (2009).

[60] W. Chu, W. A. Saidi, Q. Zheng, Y. Xie, Z. Lan, O. V. Prezhdo, H. Petek, and J. Zhao, J. Am. Chem. Soc. **138,** 13740 (2016).